RSC Advances

PAPER

View Article Online
View Journal | View Issue

Cite this: *RSC Adv.*, 2024, **14**, 27310

Strong metal-support interactions of TiO_2 interface-loaded Pt constructed under different atmospheres for adjusting the hydrogen storage reaction performance of *N*-ethylcarbazole†

Zhengjian Hou,[a] Ke Wu,[b] Huijie Wei,[a] Hua Chi,[a] Yanyan Xi,[ac] Lishuang Ma[ad] and Xufeng Lin*[ad]

In this study, two series of samples (r*T*-Pt/TiO_2 prepared with a hydrogen pretreatment and *T*r-Pt/TiO_2 prepared with an oxygen pretreatment) were prepared by treating commercial TiO_2 supports in different atmospheres to establish different TiO_2 interfacial structures, followed by the addition of platinum nanoparticles (NPs) for the catalyzed hydrogenation/dehydrogenation cycle of *N*-ethylcarbazole (NEC). The kinetic analysis and reaction mechanism were investigated by combining XRD, Raman, CO-DRIFT, HRTEM, XPS, H_2-TPD and DFT calculations. It was found that the performance of the samples for the NEC system's cyclic hydrogen storage could be modulated by treating the TiO_2 interfacial structure with different atmospheres varying the extent of strong metal-support interaction (SMSI). In addition, a turnover frequency (TOF) of 191.52 min^{-1} for dehydrogenation was achieved at 170 °C, which is better than the previously reported catalysts. Experimental studies (characterization and kinetic studies) and DFT calculations confirmed that the SMSI of the *T*r-Pt/TiO_2 series samples promoted the escape of H_2 and enhanced the catalytic activity for 4H-NEC in the 12H-NEC dehydrogenation reaction. In the NEC hydrogenation reaction, the r*T*-Pt/TiO_2 series samples were pretreated with H_2 before loading platinum metal, which led to the early activation of Ti^{4+} in their carriers, and thus suppressed the SMSI effect of the reduction process after loading platinum. This process caused the interface formed by r*T*-Pt/TiO_2 to have a higher energy barrier to 6H-NEC, which is an intermediate product of the NEC hydrogenation process, and this interrupted the hydrogenation process of 6H-NEC.

Received 8th May 2024
Accepted 8th August 2024

DOI: 10.1039/d4ra03386h

rsc.li/rsc-advances

1. Introduction

With the massive consumption of fossil fuels, global environmental and climate issues, and the imperative of carbon neutrality, hydrogen has garnered significant attention in the field of new energy sources due to its high calorific value as a fuel and its environmentally friendly characteristics.[1–3] The efficient utilization of hydrogen energy primarily involves production, storage, transportation, and utilization. Among these, hydrogen storage technology is a crucial step limiting the large-scale application of hydrogen energy in industry.[4] Over the years, various hydrogen storage technologies have been developed, including metal hydride hydrogen storage, liquid ammonia hydrogen storage, and liquid organic hydrogen carrier (LOHC) hydrogen storage.[5–8] The LOHC approach, which relies on the reversible hydrogenation and dehydrogenation of aromatic compounds, offers several advantages such as suitable hydrogen capacity, high safety, low cost, and good compatibility with existing fuel delivery infrastructure. However, many LOHC candidates, such as cyclohexane, dibenzyltoluene, and methylcyclohexane, suffer from slow hydrogen uptake/release kinetics and require relatively high storage and release temperatures.[9–11] Recent studies have shown that the introduction of nitrogen atoms can enhance the hydrogen storage performance of LOHCs at lower temperatures. In particular, *N*-ethylcarbazole (NEC) has emerged as a very promising candidate due to its desirable hydrogen storage capacity of 5.79 wt%, moderate operating temperatures (below 473 K), low volatility, and low toxicity.[12–14]

The schematic hydrogen storage steps of 12H-NEC are illustrated in Fig. 1. Cheng and Yang *et al.* investigated the kinetic performance of 12H-NEC dehydrogenation over Pd/

[a]*College of Chemistry and Chemical Engineering, China University of Petroleum (East China), Qingdao, 266580, P. R. China. E-mail: hatrick2009@upc.edu.cn; Tel: +86-532-86984695*

[b]*Changqing Engineering Design Co. Ltd, PetroChina Changqing Oilfield Company, Xi'an 710000, Shanxi, China*

[c]*Advanced Chemical Engineering and Energy Materials Research Center, China University of Petroleum (East China), Qingdao, 266580, P. R. China*

[d]*State Key Laboratory of Heavy Oil Processing, China University of Petroleum (East China), Qingdao, 266580, P. R. China*

† Electronic supplementary information (ESI) available. See DOI: https://doi.org/10.1039/d4ra03386h

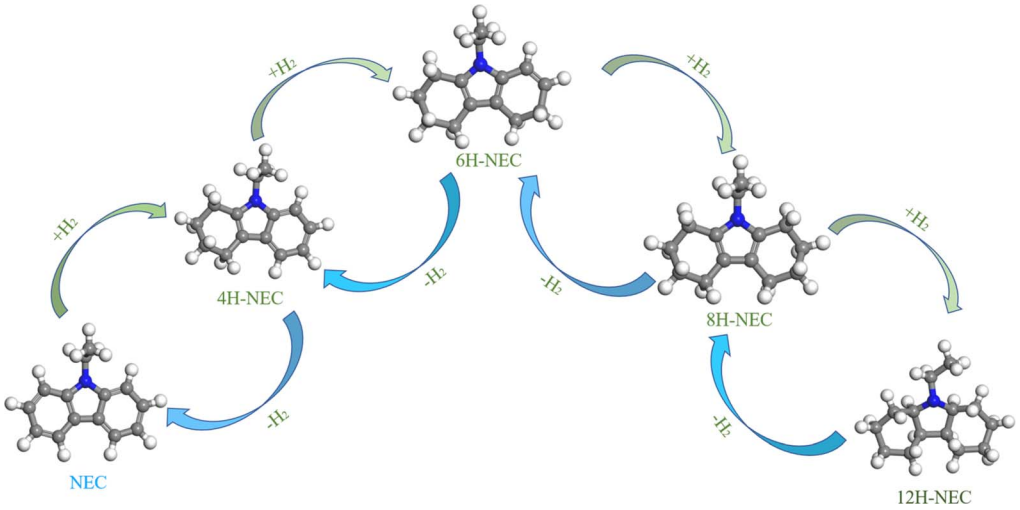

Fig. 1 Schematic diagram of the dehydrogenation/hydrogenation processes involving 12H-NEC.[12–14]

Al_2O_3 catalysts.[15,16] The dehydrogenation of 12H-NEC proceeds through three primary sequential steps: 12H-NEC to 8H-NEC, 8H-NEC to 4H-NEC, and 4H-NEC to NEC, with the conversion from 4H-NEC to 0H-NEC identified as the rate-determining step. Beyond the structural and property considerations of organic substrates, catalyst performance is pivotal for achieving efficient and cost-effective hydrogen generation and storage. To date, transition metal catalysts comprising expensive elements such as Pt, Pd, Ru, and Rh have demonstrated efficacy in the hydrogenation of NEC and dehydrogenation of 12H-NEC.[17–21] Additionally, catalysts supported on various materials, including Al_2O_3, SiO_2, activated carbon (AC), and TiO_2, have been employed in NEC-based LOHC systems.[22–26] Previous studies indicate that Ru-based catalysts exhibit superior hydrogenation performance for noble metal catalysts on inert supports, while Pd-based catalysts excel in dehydrogenation reactions.[27,28] In the context of oxide supports, Fang's group investigated the dehydrogenation activities of M/TiO_2 (M = Pt, Pd, Ru, Rh, Au) and found that Pt/TiO_2 demonstrated superior dehydrogenation properties compared to Pd.[29] Subsequent optimization of Pt content on TiO_2 revealed that 1 wt% Pt/TiO_2 exhibited optimal dehydrogenation performance, attributed to its strong metal-support interaction (SMSI) effect.[30] Furthermore, researchers successfully synthesized TiO_2 nanosheet-loaded Pt catalysts with high oxygen vacancy concentrations using solvothermal and annealing–quenching processes. These catalysts showcased excellent 12H-NEC dehydrogenation performance due to the SMSI effect.[31,32] While the outstanding dehydrogenation performance of Pt/TiO_2 due to SMSI has been established, the catalytic efficiency for NEC cyclic hydrogenation and dehydrogenation reactions remains underreported. Additionally, developing cost-effective Pt/TiO_2 catalysts for LOHC applications is crucial.

In order to address these issues, in this study, two series of samples (r*T*-Pt/TiO_2 and *T*r-Pt/TiO_2, used for hydrogen uptake of NEC and release of 12H-NEC, respectively) were prepared by treating commercial TiO_2 supports in different atmospheres to build up different TiO_2 interfacial structures, and then loading platinum nanoparticles (NPS). Kinetic analysis and reaction mechanism were investigated by combining XRD, RAMAN, CO-DRIFT, HRTEM, XPS, H2-TPD and DFT. It was found that the performance of the samples in the NEC cyclic dehydrogenation reaction can be tuned by treating the TiO_2 interface structure with different atmospheres and utilizing temperature-controlled SMSI. In addition, the turnover frequency (TOF) at 170 °C reached 191.52 min^{-1}, which was superior to previously reported catalysts.[30] Both the experimental studies (characterization and kinetic studies) and the DFT calculations confirmed that for the 12H-NEC dehydrogenation reaction, SMSI of the *T*r-Pt/TiO_2 series samples promotes H_2 escape and improves the catalytic activity towards 4H-NEC. In the reaction of NEC hydrogenation, the r*T*-Pt/TiO_2 series samples were pretreated with H_2 before loading platinum metal, which led to the initial activation of Ti^{4+} in their carriers, thus inhibiting the SMSI effect of the reduction process after loading platinum. This process gives the interface formed by r*T*-Pt/TiO_2 a higher energy barrier to 6H-NEC, an intermediate product of the NEC hydrogenation process, which interrupts the excessive competition for adsorption during the hydrogenation process and makes it easier to adsorb and dissociate H_2 due to the lower dissociation energy barrier of H_2 at the time of the hydrogenation reaction.

2. Experimental section

2.1. Chemicals

N-Ethylcarbazole (97%) was purchased from Aladdin and used as a hydrogenation reactant. $H_2PtCl_6 \cdot 6H_2O$ and isopropyl alcohol (A.R. >99.7%) were purchased from the Sinopharm Chemical reagent Co., Ltd. P25 was purchased from Degussa Co., Ltd. All atmospheres used are of ultra-pure grade (>99.99).

2.2. Catalyst preparation

P25 was used as a support and treated with air or hydrogen at 350 °C and labeled as O–TiO_2 and H–TiO_2, respectively. Metal component loading *via* a wetness vacuum impregnation

method. In detail, a platinum precursor solution was formed by dissolving 0.162 g of H_2PtCl_6 in 2.4 g of water (the amount of water was determined based on an equal volume impregnation of 3.0 g of support). The Pt precursor solution was then vacuum impregnated with 3.0 g of O–TiO_2 and H–TiO_2 powders, respectively, overnight. The impregnated samples were vacuum dried at 120 °C for 4 hours. All the above samples were calcined in H_2 at 300 °C, 400 °C, and 500 °C for 4 h with a heating rate of 5 °C min^{-1} from room temperature. The samples obtained using O–TiO_2 support and H–TiO_2 support are referred to as *T*r-TiO_2 and r*T*-TiO_2, respectively ($T = 300$, 400, 500).

For easier reading, the parts of Catalyst characterization, NEC hydrogenation and 12H-NEC dehydrogenation reaction testing, and theoretical calculations are described in the ESI.†

3. Results and discussion

3.1. Characterization of catalysts

To gain deeper insights into the evolution of the TiO_2 chemical state under various atmosphere treatments, X-ray photoelectron spectroscopy (XPS) was employed to meticulously analyze the surface chemistry of the samples, as depicted in Fig. 2. Notably, characteristic peaks centered around 458 eV and 464 eV, attributed to the Ti $2p_{3/2}$ and Ti $2p_{1/2}$ orbitals, respectively, were consistently observed across all prepared samples. Comparative analysis revealed a slight decrease (~0.1–0.4 eV) in the binding energies of Ti $2p_{3/2}$ and Ti $2p_{1/2}$ compared to those of the P25 support (~458.47 eV and ~464.28 eV), indicative of electron gains in the Ti 2p orbitals and a reduction in some titanium valence states (Fig. 2a). Similarly, the O 1s orbital peaks, located near 529 eV in all samples, also exhibited a marginal decrease (~0.1–0.4 eV) in binding energy relative to the O 1s peak observed at 529.70 eV in the P25 support, suggesting enhanced electron coordination of surface oxygen atoms (Fig. 2b). Upon closer examination, samples subjected to hydrogen treatment prior to loading displayed relatively smaller reductions in Ti 2p and O 1s binding energies compared to those treated with oxygen. Moreover, as treatment temperatures increased, the reductions in Ti 2p and O 1s binding energies became more pronounced. The Ti $2p_{3/2}$ binding energy notably shifted to

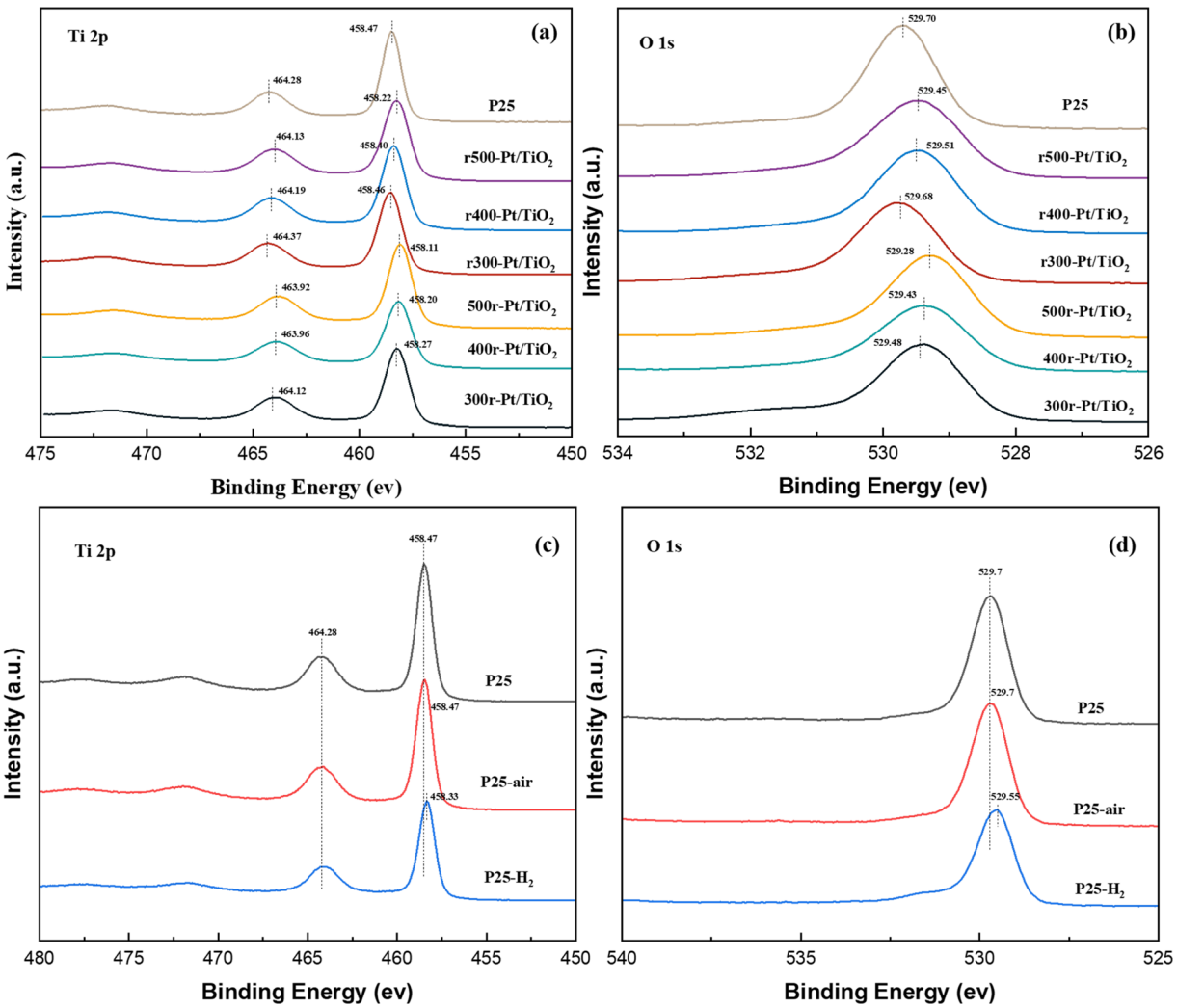

Fig. 2 Ti 2p and O 1s XPS spectra of the prepared samples ((a) Ti 2p of prepared samples, (b) O 1s of prepared samples, (c) Ti 2p of P25 treated with different gases, (d) O 1s of P25 with different gas treatments).

lower values following high-temperature reduction, attributed to the phase transformation of TiO_2 in the SMSI state to Ti_4O_7, a well-documented phenomenon in catalysis.[33,34] In the case of the O 1s XPS spectrum, it is a typical convolution of the lattice O peaks and the surface hydroxyl peaks. The slight redshift of the O 1s peaks is mainly attributed to two reasons, firstly, the reduction of surface hydroxyls in all of the samples treated with high temperature in hydrogen compared to the clean P25.[35] The second reason is that the hydrogen treatment causes a portion of the oxygen on the surface to escape and rearrange during the electron gain outside the Ti orbitals during the SMSI process in order to cause the formation of oxygen defects. Compared to the r*T*-Pt/TiO_2-like samples that have been reloaded by hydrogen pre-treatment of P25, the air pre-treated *T*r-Pt/TiO_2-like form Ti–Pt–O escaping more O, resulting in a larger red-shift.[36,37] In order to understand this behavior more clearly, an XPS energy spectrum analysis was performed on samples of P25 treated at 350 °C under different atmospheres, as shown in Fig. 2c and d. It can be seen that the Ti $2p_{3/2}$ binding energy of the hydrogen-treated P25 supported is red-shifted, indicating that the Ti^{4+} on the carrier surface is partly converted to Ti^{3+}(Fig. 2c). For O 1s the binding energy of hydrogen-treated P25 support P25-H_2 also undergoes a redshift of ~0.15 eV (Fig. 2d), which suggests that both surface lattice oxygen and surface oxygen hydroxyl groups escape under hydrogen treatment. In contrast, there was no significant difference between the oxygen-treated P25 and the P25 dried under argon.

For SMSI formed on the stable Pt nanoclusters, the amount of oxygen vacancies in the oxide support is an important factor for the generation of anchor localization sites.[38,39] Fig. 3a–d shows the Raman E_g peaks of the above prepared samples. The position of the asymmetric peaks tends to correlate with the number of defects in the lattice.[40,41] The E_g vibrational mode observed in the Raman spectrum is intrinsically linked to planar oxygen–oxygen (O–O) interactions, rendering it particularly sensitive to the presence of oxygen defects within the TiO_2

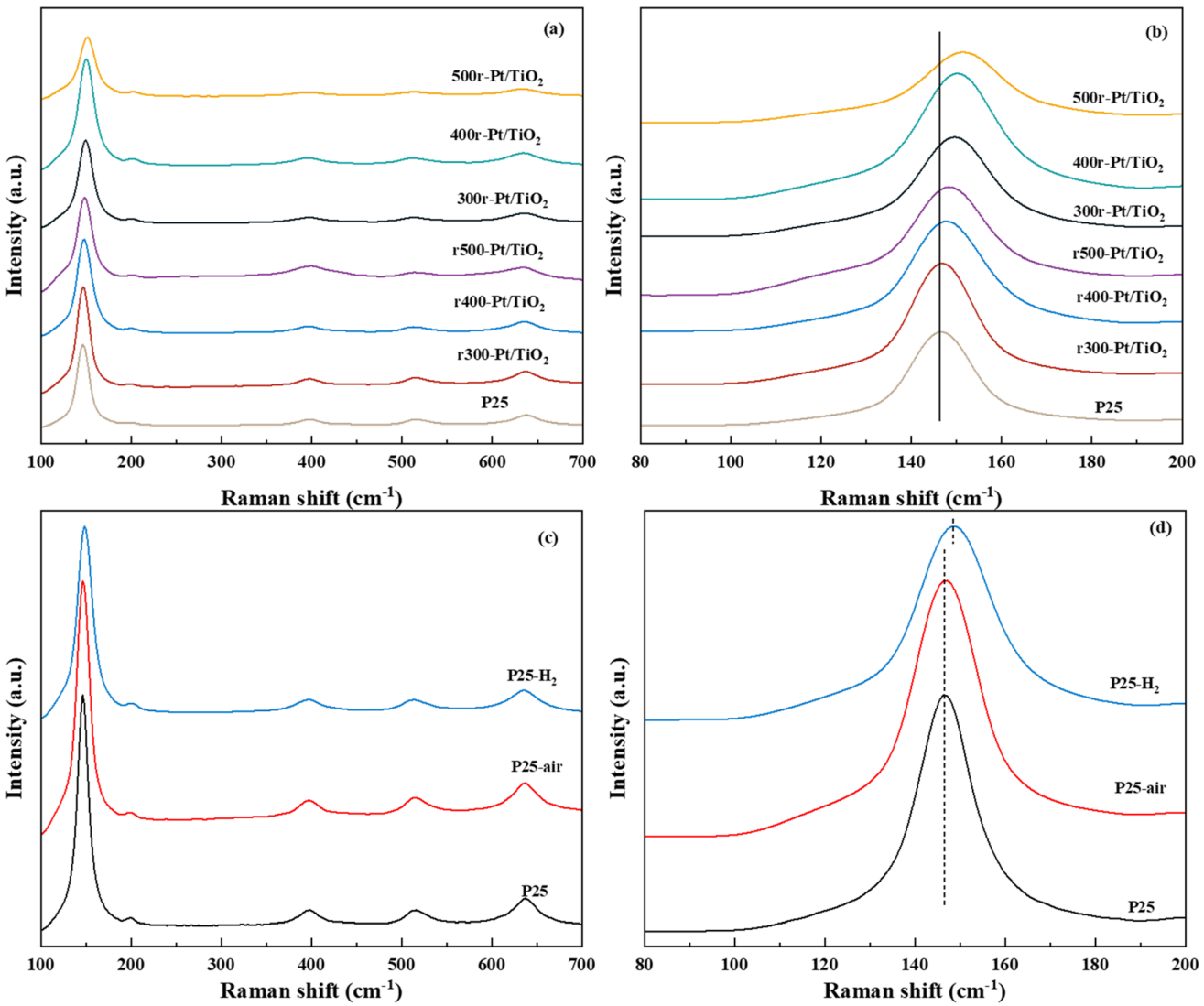

Fig. 3 Raman spectra of samples ((a) spectra at 100–700 cm^{-1}, (b) spectra at 80–200 cm^{-1}, (c) spectra at 100–700 cm^{-1} and (d) 80–200 cm^{-1}, respectively).

lattice. By analyzing the correlation between the peak position and the full width at half-maximum (FWHM) of the most intense E_g mode, typically found around 146 cm^{-1}, the concentration of oxygen vacancies can be quantitatively assessed.[42,43] This methodological approach enables a detailed evaluation of the structural and electronic modifications in TiO_2, thereby providing critical insights into the material's defect dynamics and their implications on its functional properties. The Raman E_g peak position (violet spectrum) for r300-Pt/TiO_2 is nearly identical to that of P25, whereas the peaks for r400-Pt/TiO_2 and r500-Pt/TiO_2 exhibit slight shifts towards higher wavenumbers. In contrast, the Raman E_g peaks of the *T*r-Pt/TiO_2 series samples demonstrate significant shifts to higher wavenumbers, with a clear pattern: the higher the reduction temperature of the metal, the larger the shift (500r-Pt/TiO_2 > 400r-Pt/TiO_2 > 300r-Pt/TiO_2). This observation suggests that the higher the formation temperature, the greater the number of oxygen vacancies formed on the surface. Furthermore, it indicates that as the temperature increases, more electron migration occurs from TiO_x to Pt. To gain a deeper understanding of this phenomenon, the plots of the proppant before different atmosphere treatments at the same temperature were analyzed to investigate changes in surface oxygen defects (Fig. 3c and d). The three curves intuitively show that, compared to the inert gas-dried and oxygen-treated P25 with the peak center at approximately 145 cm^{-1}, the hydrogen-treated P25–H_2 exhibits a significant shift to around 152 cm^{-1}. This shift indicates that hydrogen treatment can effectively promote the generation of oxygen defects on the surface of P25.

The XPS energy spectrum of Pt 4f is shown in Fig. 4a, where Pt exists mainly in the metallic state. For all samples, the orbital energy spectra of the asymmetric peaks located at ~70.2–70.3 eV and ~73.5–74.9 eV correspond to Pt $4f_{7/2}$ and Pt $4f_{5/2}$, respectively. The binding energy of Pt $4f_{5/2}$ compared to all samples decreases with the increasing reduction temperature, which is a result of electron transfer from TiO_2 to Pt as the work function of Pt is higher than that of TiO_2.[44–46] The difference in the extent of the SMSI effect between Pt and TiO_2 and the gradual transformation of TiO_2 into TiO_x during hydrogen reduction results in a different number of electrons in the Pt 4f orbitals, and the more obvious the SMSI effect is, the lower the binding energy becomes, and the more electrons are gained in the Pt 4f

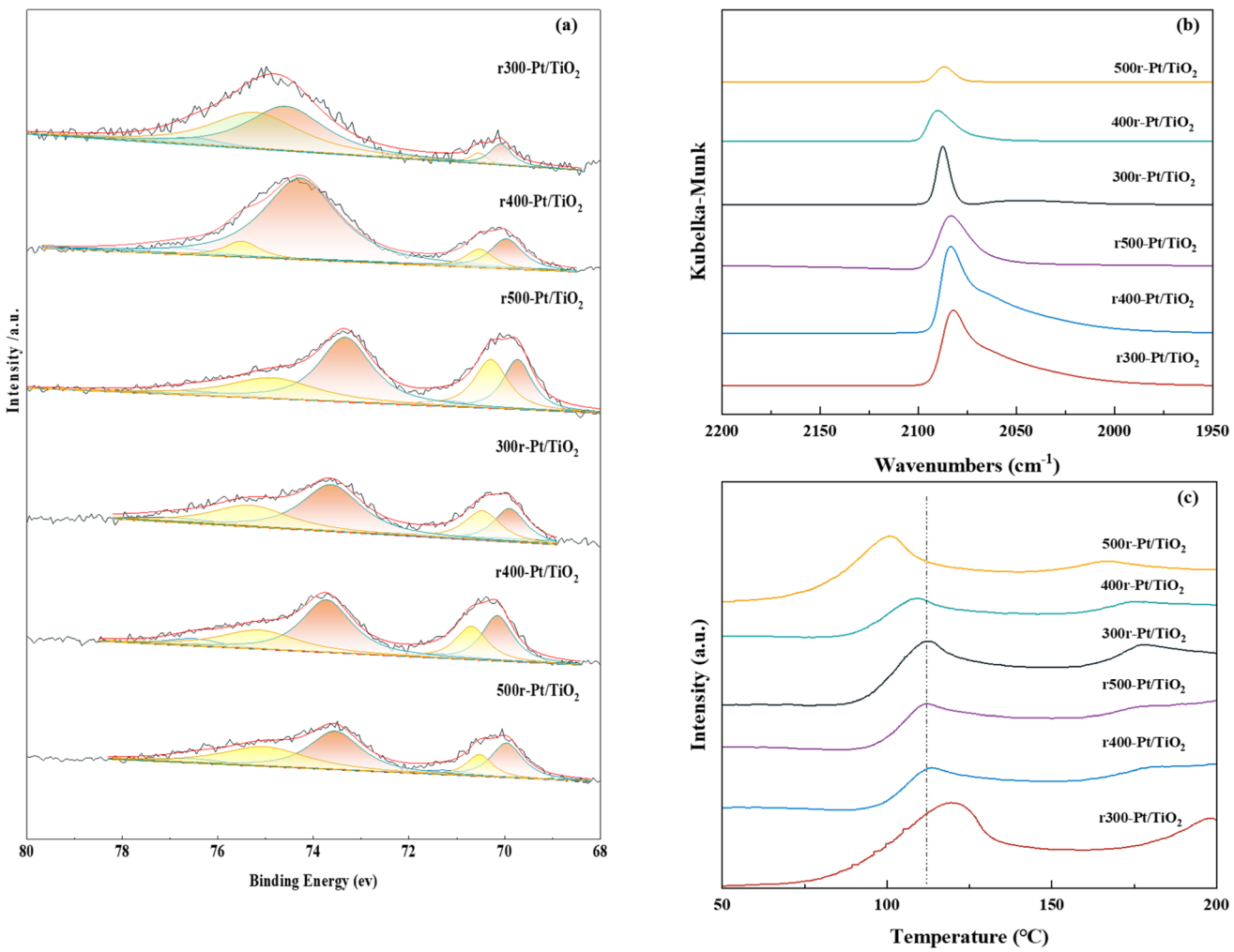

Fig. 4 Pt 4f XPS spectra (a), *in situ* CO-DRIFT spectra (b), H_2-TPD profiles (c) of the prepared sample.

orbitals.[47] In this study, as the hydrogen treatment temperature increases, the lower the binding energy, the more serious the SMSI. While comparing the r*T*-Pt/TiO_2 and *T*r-Pt/TiO_2 series prepared by hydrogen and air treatment pretreatment carriers, it is obvious that the binding energy of the r*T*-Pt/TiO_2 series is higher than that of the *T*r-Pt/TiO_2 after the temperature reduction treatment, which indicates that the hydrogen pretreatment carriers can effectively prevent the migration of electrons from the Ti outer electrons to the Pt electrons during the reduction of Pt metal by hydrogen and reduce the degree of SMSI.

In situ CO-DRIFT spectroscopy was performed to explore the adsorption properties and electronic structure of the Pt surface at room temperature, and the results are shown in Fig. 4b. In all the prepared samples, it can be observed a peak centered at ~2060–2089 cm^{-1}, that corresponds to a CO molecule linearly adsorbed on the Pt (111) platform site with a coordination number of 9.[48,49] In contrast to the narrow peak centered at 2085–2089 cm^{-1} for the *T*r-Pt/TiO_2 series samples, a bandwidth peak extending to ~2070 cm^{-1} appears on the r*T*-Pt/TiO_2 series which is attributed to the linearly adsorption of CO molecules on the low-coordinated edge and corner Pt sites. This behavior also suggests that a portion of the Pt may fall on O vacancies generated by TiO_2 escaping oxygen and hydroxyl groups during hydrogen treatment of the P25 supported, as analyzed above. In addition, the CO-DRIFTS analysis provides information on the Pt metal exposure on the sample surface in a semi-quantitative format. Numerous studies have demonstrated that the inhibition of small molecule adsorption (*e.g.*, CO, H_2) in the presence of SMSI is a characteristic phenomenon.[50–52] Consequently, CO-DRIFTS can be effectively utilized to evaluate the extent of SMSI in various samples. As is apparent from Fig. 4b, the adsorption of CO on Pt in the r*T*-Pt/TiO_2 series of samples increases compared to *T*r-Pt/TiO_2 using reduced Pt NPs at the same temperature. The relatively low adsorption strength of CO on *T*r-Pt/TiO_2 is explained by the fact that the metal Pt particles are partially covered by a layer of TiO_x, suggesting that the pretreatment of the P25 support with hydrogen can effectively inhibit the SMSI behavior. As the temperature increases from 300 to 500 °C under the same atmosphere pretreatment, the adsorption of CO on Pt decreased, which indicates that the higher the temperature of the treated reduced Pt NPs, the more severe the partial coverage of TiO_x due to the SMSI effect. Among the r*T*-Pt/TiO_2 series samples the same pattern happened, which is a result of the fact that the pretreated support.

A hydrogen overflow state of Pt on the sample surface was investigated by H_2-TPD, as shown in Fig. 4c. In the past, chemisorbed hydrogen in samples tended to desorb reversibly at 150–200 °C.[53,54] Comparison of the H_2 desorption curves shows that the hydrogen overflow capacity of the samples increases (*i.e.*, adsorption of hydrogen decreases) as the temperature of the reduced Pt increases and the temperature of the sample hydrogen overflow decreases. In particular, the r300-Pt/TiO_2 sample has the strongest capacity for hydrogen adsorption, while the 500r-Pt/TiO_2 sample has the strongest capacity for hydrogen overflow. This behavior also suggests that the SMSI effect promotes the occurrence of hydrogen overflow.

The H_2 chemisorption analysis is a highly valuable characterization technique for systems exhibiting the SMSI effect. In these systems, an intensified SMSI effect results in reduced H_2 chemisorption capability of the metal nanoparticles. Therefore, it is crucial to quantify the H_2 uptake of each sample through H_2 chemisorption to provide a clear understanding of the SMSI effect's impact on the catalytic properties of the samples. Comparing the hydrogen adsorption peaks of the samples reveals distinct trends: for r*T*-Pt/TiO_2 catalysts treated with hydrogen prior to Pt reduction, the area of the hydrogen adsorption peak diminishes noticeably at equivalent Pt reduction temperatures. Conversely, catalysts subjected to identical carrier treatments exhibit reduced hydrogen adsorption peak areas as the Pt reduction temperature increases. These observations underscore the effectiveness of hydrogen pretreatment in mitigating the SMSI between Pt and TiO_x.

For observing the SMSI between Pt clusters and TiO_2 supports in the samples, HRTEM was utilized as shown in Fig. 5. In all samples, TiO_2 exposed surface is dominated by the (101) surface, while Pt clusters exposed surface is dominated by the (111) surface. Meanwhile, it can be clearly seen that the Pt NPs are directly supported on the TiO_2 surface. After the reduction of r*T*-Pt/TiO_2 and *T*r-Pt/TiO_2, the Pt NPs are wrapped by metal oxides as shown in the HRTEM images, and the wrapping occurring through SMSI can be regarded in the process of Pt NPs being "wetted" by the reduced metal oxides. Such process is mainly driven by the surface tension factor, which is expected to be higher for metals than for metal oxides. This wetting behavior becomes more severe with higher temperatures of reduced Pt (*e.g.* c > b > a and f > e > d). In addition, it can be clearly seen that the amount of Pt NPs encapsulated by TiO_x is reduced in r*T*-Pt/TiO_2 compared to *T*r-Pt/TiO_2.

Combined with the above series of sample characterization tests, a certain difference in the surface structure of the samples obtained by loading P25 with Pt NPs in different atmospheres can be clearly analyzed, which is mainly manifested in the distribution of oxygen defect sites and Ti–OH on the surface of the samples. Different from the r*T*-Pt/TiO_2 series samples prepared by hydrogen-treated P25, the *T*r-Pt/TiO_2 series samples prepared by air-treated P25 have fewer oxygen defects on the surface, which was replaced by more Ti–OH, and this change makes the interfacial structure of the two samples fundamentally different. Specifically, as shown in Fig. 5, the Pt loading process of the air-treated P25-prepared *T*r-Pt/TiO_2 series samples combined with Ti–O–H at the interface to form a Ti–O–Pt structure. In contrast, the hydrogen-treated support resulted in a Ti–Pt interfacial structure as a result of the generation of oxygen defects and the removal of Ti–OH during hydrogen treatment. On the other hand, the majority of the TI^{4+} capable of migrating at the interface has been activated in advance by the hydrogen reduction treatment of the P25 support before loading the Pt precursor in the r*T*-Pt/TiO_2 series samples, which leads to only a small amount of TI^{4+} migrating to the Pt NPS at the interface during the Pt metal reduction process resulting in the reduction of the Pt coverage due to the SMSI effect.

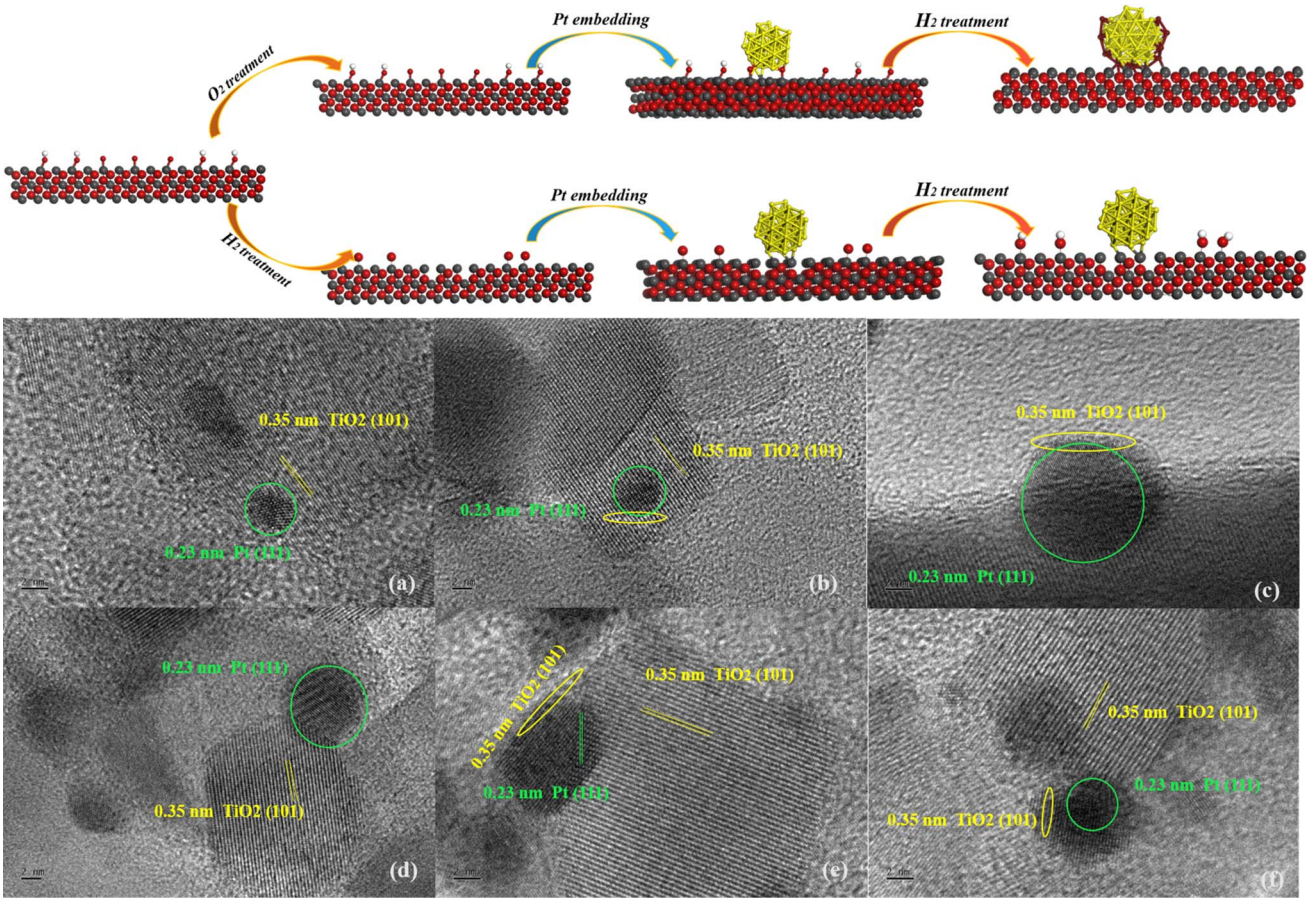

Fig. 5 HRTEM images of (a) r300-Pt/TiO_2, (b) r400-Pt/TiO_2, (c) r500-Pt/TiO_2, (d) 300r-Pt/TiO_2, (e) 400r-Pt/TiO_2, and (f) 500r-Pt/TiO_2 (all image scale bars are 2 nm in this figure).

3.2. Hydrogenation and dehydrogenation reaction tests

Fig. 6a and b Show the selectivity of six different samples for the complete hydrogenation product (12H-NEC) at different temperatures and the hydrogen consumption for 2 h of hydrogenation at 130 °C. The efficiency of hydrogenation of the samples under NEC at different temperatures is tested, and it can be directly observed that the r*T*-Pt/TiO_2 series samples have higher hydrogenation efficiency than *T*r-Pt/TiO_2, while hydrogenation efficiency increases with the increase of temperature (Fig. 6a). Desorption of H_2 adsorption by Pt is a speedy process. The hydrogen consumption of different samples for catalytic NEC hydrogenation at 130 °C is shown in Fig. 6b. At 130 °C, all six samples display completely different hydrogen consumption curves. In detail, the r*T*-Pt/TiO_2 series of samples consumed more hydrogen at 2 h, and the first inflection point at ~60 min indicated a stronger adsorption and dissociation of hydrogen. In contrast, the *T*r-Pt/TiO_2 series samples have lower hydrogen uptake throughout the hydrogenation process, with the saturation inflection point occurring after ~80 min, with 500r-Pt/TiO_2 consuming the lowest amount of hydrogen. It could be related to the deeper SMSI effect of the *T*r-Pt/TiO_2 series samples after high-temperature reduction as determined by the previous sample characterization above, which has been the adsorption of small molecules of hydrogen.

Fig. 6c and d Show the selectivity of six different samples for the total dehydrogenation product (NEC) at different temperatures and the hydrogen release from the dehydrogenation at 170 °C for 6 h. The dehydrogenation efficiencies of the samples under NEC conditions at different temperatures were test, and it can be directly observed that the dehydrogenation efficiency of the *T*r-Pt/TiO_2 series of samples is higher than that of r*T*-Pt/TiO_2, while the dehydrogenation efficiency increases with the increase of temperature (Fig. 6d). Similarly, the adsorption and desorption of H_2 by Pt is a rapid process. The hydrogen release from different samples catalyzing the dehydrogenation of 12H-NEC at 170 °C is shown in Fig. 6d. The hydrogen release profiles of all six samples at 170 °C are completely different. Specifically, the *T*r-Pt/TiO_2 series of samples released more hydrogen within 6 h. The first inflection point at ~180 min indicates stronger adsorption and dissociation of hydrogen. In contrast, the r*T*-Pt/TiO_2 series of samples released less hydrogen throughout the hydrogenation process, with the saturation inflection point occurring after ~210 min, with r300-Pt/TiO_2 having the lowest hydrogen consumption. This may be related to the deeper SMSI effect (*i.e.*, inhibition of adsorbed small-molecule hydrogen). After high-temperature reduction of the *T*r-Pt/TiO_2 series samples, as determined by the sample characterization above. The strongest catalytic dehydrogenation performance of the

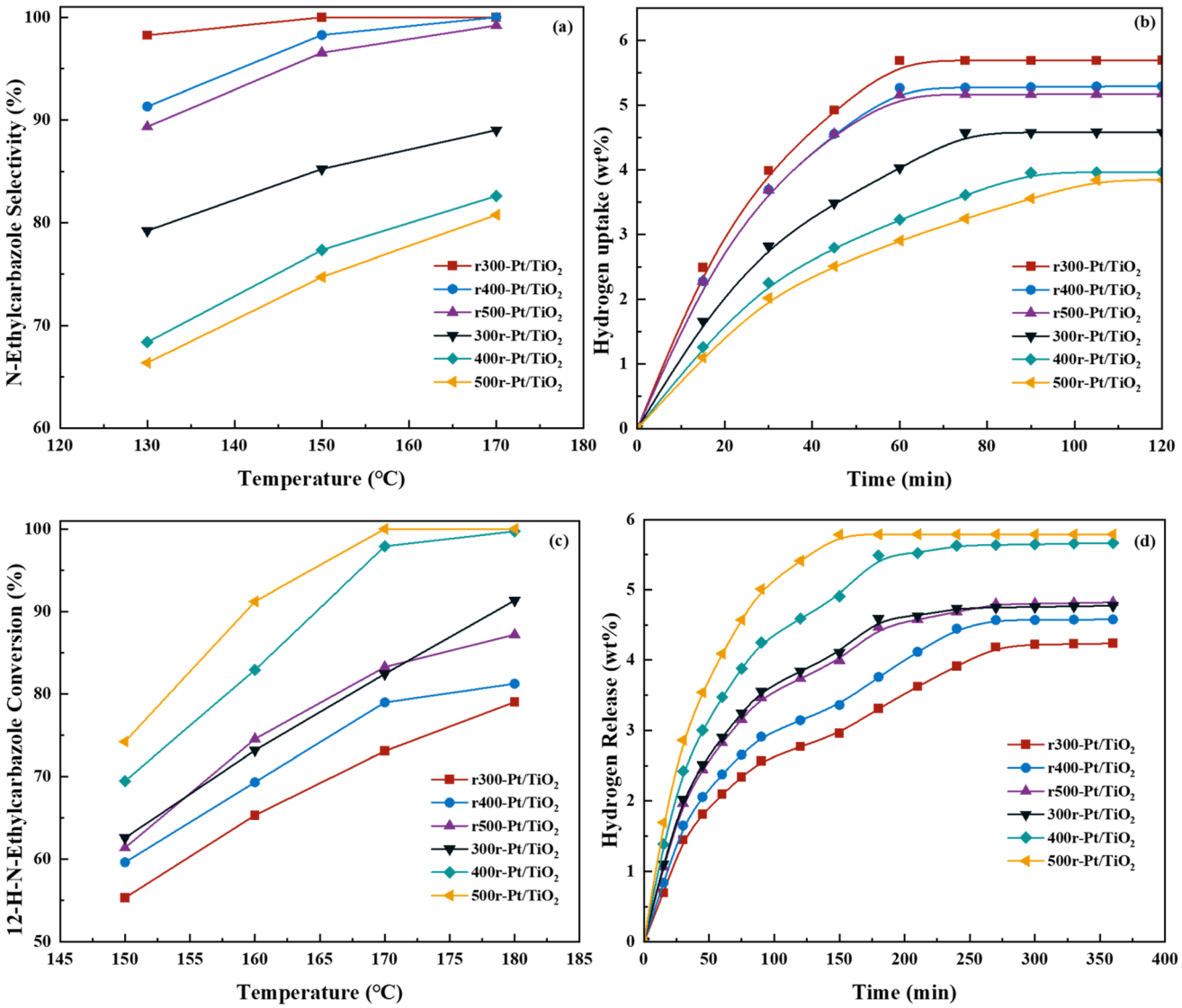

Fig. 6 Catalytic characterization of NEC hydrogenation (a) selectivity of 12H-*N*-ethylcarbazole from the full hydrogenation at different reaction temperatures (b) H_2 uptake profile at 130 °C (reaction pressure 6 MPa, reaction time 2 h and reaction speed 1200 rpm), NEC dehydrogenation (c) selectivity of *N*-ethylcarbazole after full dehydrogenation at different reaction temperatures (reaction time 2 h reaction speed 1200 rpm) (d) H_2 releases profile at 170 °C (reaction pressure under atmospheric, reaction time 6 h and reaction speed 1200 rpm).

500r-Pt/TiO_2 samples is related to their strongest SMSI effect as a result of sample characterization.

For a more profound understanding of the changes in all samples during the hydrogenation process, Fig. S5† shows the curves of the concentration of the intermediates during the hydrogenation process. In all of the analyzed intermediates, the concentration of 4H-NEC increased with reaction time when NEC was first hydrogenated to 4H-NEC, with the r*T*-Pt/TiO_2 series peaking faster than the *T*r-Pt/TiO_2 series (r*T*-Pt/TiO_2 series peaking at ~20 min and *T*r-Pt/TiO_2 series at ~30–40 min). For all samples the lower the metal reduction temperature the faster the 4H-NEC depletion and accumulation (*e.g.* r300-Pt/TiO_2 > r400-Pt/TiO_2 > r500-Pt/TiO_2 and 300r-Pt/TiO_2 > 400r-Pt/TiO_2 > 500r-Pt/TiO_2). The gradual hydrogenation of 4H-NEC leads to the generation of 8H-NEC, in which the r*T*-Pt/TiO_2 series gradually saturates with 4H-NEC and starts to consume it all at about 45 min, and the concentration of 8H-NEC accumulates to the peak. On the other hand, the concentration of the 8H-NEC in the *T*r-Pt/TiO_2 series increases slowly until the 4H-NEC is consumed at about 80 min, and the concentration of 8H-NEC accumulates to the peak, and then decreases slowly. Combined with Fig. 6b, it can be analyzed that the accumulation and consumption of 4H-NEC may be mainly influenced by the rate of H_2 adsorption and dissociation on the sample. Meanwhile, with the saturated accumulation of 8H-NEC followed by hydrogenation and depletion, the r*T*-Pt/TiO_2 series underwent a rapid depletion at the peak of 8H-NEC concentration (slope of the curve r400-Pt/TiO_2 > r500-Pt/TiO_2), but obviously the rate of 8H-NEC depletion in *T*r-Pt/TiO_2 is much lower than that of the r*T*-Pt/TiO_2 series. This behavior suggests

that the depletion of hydrogenation and the accumulation of 8H-NEC may be related to the adsorption–dissociation equilibrium of 8H-NEC in the sample itself. Comparing the 12H-NEC, it can be more intuitively found that the generation rate of r*T*-Pt/TiO_2 series is faster (r300-Pt/TiO_2 > r400-Pt/TiO_2 > r500-Pt/TiO_2), with an inflexion point at about 80–100 min, whereas the concentration of 12H-NEC in the samples of the *T*r-Pt/TiO2 series continues to increase slowly (300r-Pt/TiO_2 > 400r-Pt/TiO_2 > 400r-Pt/TiO_2) until the end of the reaction at 120 min.

Similarly, in order to gain more insight into the behavior of all samples during the dehydrogenation process, Fig. S6† shows the concentration profiles of the intermediates during the dehydrogenation process. For all analyzed intermediates, when 12H-NEC was first dehydrogenated to 8H-NEC, the concentration of 8H-NEC accumulated with the reaction time, with the *T*r-Pt/TiO_2 series accumulating to the peak faster than the r*T*-Pt/TiO_2 series (*T*r-Pt/TiO_2 series peaked at ~70 min and rapidly consumed at 120–180 min, *T*r-Pt/TiO_2 series peaked at ~120 min and rapidly depleted in 120–240 min). For all samples, the higher the metal reduction temperature, the faster the consumption and accumulation of 8H-NEC (*e.g.*, 500r-Pt/TiO_2 > 400r-Pt/TiO_2 > 300r-Pt/TiO_2 and r500-Pt/TiO_2 > r400-Pt/TiO_2 > r300-Pt/TiO_2). The gradual dehydrogenation of 8H-NEC led to the accumulation of 4H-NEC, in which 4H-NEC in the *T*r-Pt/TiO_2 series was gradually saturated and began to be dissipated at about 80 min. On the other hand, the NEC concentration in the *T*r-Pt/TiO_2 series increased slowly until 4H-NEC no longer accumulated at about 80 min, and the NEC concentration increased rapidly, with residual 4H-NEC in the 300r-Pt/TiO_2. In contrast, in the r*T*-Pt/TiO_2 series, the time to complete large-rate dehydrogenation of 8H-NEC tends to be later (after ~150 min) and the slope decreases with decreasing metal reduction temperature. In addition, the presence of 8H-NEC was found eventually in both r300-Pt/TiO_2 and r300-Pt/TiO_2. For all samples, there is a depletion of 8H-NEC and the rate of NEC generation increases substantially. Combine with Fig. 5d, it can be analyzed that the decisive step of the reaction is 8H-NEC to 4H-NEC (rapid adsorption of 8H-NEC is converted to 4H-NEC and then desorbed).

The dehydrogenation reaction was then studied quantitatively. According to the literature, the 12-NEC dehydrogenation reaction can be described as three basic reactions:[55,56]

$$12\text{H-NEC} \xrightarrow{k_1} 8\text{H-NEC} + 2H_2$$

$$8\text{H-NEC} \xrightarrow{k_2} 4\text{H-NEC} + 2H_2$$

$$4\text{H-NEC} \xrightarrow{k_3} \text{NEC} + 2H_2$$

where k_1, k_2 and k_3 represent the rate constants for the three basic reactions, respectively, as calculated in the ESI.† The results of the kinetic reaction rate constant calculations are presented in Table 1. Comparing the different samples, it is observed that the order of magnitude of k_3 is much smaller than the other two for all samples, which also indicates that the conversion of 4H-NECZ during the reaction limits the dehydrogenation reaction. Meanwhile, TOF values were calculated for comparing the activities of different samples. The size of the TOF values were compared and the *T*r-Pt/TiO_2 series was more active in the dehydrogenation reaction, with 500r-Pt/TiO_2 having the best activity. Combined with the dispersion of different samples and the previous analysis of sample properties, it shows that the reaction temperature affects the sample SMSI effect (the higher the temperature of reduced Pt, the stronger the SMSI effect), and the dehydrogenation activity of the samples in 12H-NEC is further improved with the enhancement of the SMSI effect. Furthermore, when compared to the data reported in the past literature,[30] the samples treated

Table 1 Catalytic dehydrogenation activity data in 360 min at 170 °C and partial characterization results of sample

Sample	Dispersion[a] (%)	ICP-MS metal[b] (wt%)	Rate constant k_1 (min^{-1})	Rate constant k_2 (min^{-1})	Rate constant k_3 (min^{-1})	TOF (min^{-1})	T (°C)	Ref.
300r-Pt/TiO_2	16.93	1.95	0.023	0.016	0.006	93.29	170	—
400r-Pt/TiO_2	13.75	1.92	0.030	0.018	0.009	152.16	170	—
500r-Pt/TiO_2	11.23	1.93	0.031	0.019	0.011	191.52	170	—
r300-Pt/TiO_2	25.82	1.91	0.014	0.010	0.001	38.01	170	—
r400-Pt/TiO_2	21.37	1.97	0.016	0.013	0.001	50.89	170	—
r500-Pt/TiO_2	19.11	1.97	0.022	0.014	0.004	78.25	170	—
1.0wt%Pt/TiO_2	24.87	0.95	0.017	0.014	0.003	95.98	170	30
1.0wt%Pt/TiO_2	24.87	0.95	0.046	0.029	0.012	259.73	180	30
2.5wt%Pt/TiO_2	12.39	2.46	0.044	0.031	0.011	172.27	180	30
Pd/SiO_2	4.21	4.79	0.028	0.019	0.003	106.6	180	22
Pd_3Cu_1/SiO_2	4.03	3.72	0.052	0.023	0.005	199.9	180	13
Ni_6@Pd_1-R(6)/M41	—	—	—	—	—	84.6	180	24
Pd-IP/S15	70	—	—	—	—	13.94	170	57
Pd-WP/S15	66	—	—	—	—	2.63	170	57
Pd-WC/S15	25	—	—	—	—	2.19	170	57
Pd/C	38	—	—	—	—	1.36	170	57

[a] Data from CO chemisorption. [b] Data from ICP-MS.

directly under hydrogen at 400 °C were more dehydrogenated than the samples reduced with 1.0 wt% Pt/TiO_2 and 2.5 wt% Pt/TiO_2 sodium citrate (at 170 °C, the 400r-Pt/TiO_2 and 500r-Pt/TiO_2 samples were more advantageous both in terms of the TOF values and reaction rate).

For further understanding of the adsorption mode of 12H-NEC on the samples, DRIFT spectroscopy was used to investigate the surface adsorption behavior of the samples using 12H-NEC as a probe molecule in the present study. The *in situ* CAL-DRIFT spectra of different samples are shown in Fig. 7. All samples showed four signal peaks in the upper 12H-NEC, in which 2851 cm^{-1}, 2930 cm^{-1}, 2974 cm^{-1} and 3051 cm^{-1} were attributed to the C–H_2 symmetric stretching mode, the C–H_2 asymmetric stretching mode, the C–H_3 asymmetric stretching mode, and C–H vibration on the aromatic ring, respectively. In addition, in the lower frequency bands 1480 cm^{-1},1453 $cm^{-1}$and 1325 cm^{-1} were also found to arise on the samples, attributed to C–C symmetry vibrations on the benzene ring, C–C symmetry vibrations on the five-membered ring, and C=C symmetry stretching vibrations on the five-membered ring, respectively. Specifically, it is illustrated that there are no C–H vibrational markers caused by dehydrogenation of the five-membered ring near ~1550 cm^{-1} throughout the spectrum, indicating that no dehydrogenation reaction occurred throughout the sample treatment.[58] These characteristic peaks indicate that 12H-NEC adsorbs on the prepared samples in a manner consistent with past reports of adsorption on Pt, which are all lying flat on the sample interface.[59,60]

3.3. Hydrogenation and dehydrogenation reaction tests

In-depth insights into the chemical dynamics of *T*r-Pt/TiO_2 and r*T*-Pt/TiO_2 models were achieved through detailed DFT calculations, elucidating their respective roles in the reversible hydrogenation–dehydrogenation reactions of 12H-NEC. Fig. S6 and S7† illustrate the structural models used in these calculations, revealing critical reaction pathways and energy profiles during these processes. Central to the performance of these catalytic systems is the adsorption behavior of substrate molecules and the dissociative synthesis of hydrogen, pivotal aspects addressed in Fig. 8. Fig. 8a delineates the adsorption energies of NEC and its derivatives (*n*H-NEC, where $n = 4, 6, 8, 12$) on r-Pt/TiO_2 and r*T*-Pt/TiO_2 surfaces, alongside the dissociation of hydrogen ions. Notably, *n*H-NEC exhibits significantly higher adsorption energies on the *T*r-Pt/TiO_2 surface compared to r*T*-Pt/TiO_2, suggesting stronger interactions that facilitate enhanced 12H-NEC dehydrogenation efficiencies (see Table S3† for comprehensive data). Specifically, the energy profiles across various reaction stages highlight the critical role of the 4H-NEC to NEC transition, where r*T*-Pt/TiO_2 demonstrates a lower energy requirement (−0.37 eV) compared to r-Pt/TiO_2 (−0.17 eV), underscoring superior adsorption properties conducive to the dehydrogenation process. Moreover, Fig. 8b details the hydrogen dissociation process on these surfaces. Activation barriers for H–H bond dissociation (TS1) are notably higher on *T*r-Pt/TiO_2 (0.32 eV) compared to r*T*-Pt/TiO_2, possibly attributed to differences in Ti–Pt *versus* O–Pt interfacial electron arrangements. Subsequent steps involving Pt–H bond formation and hydrogen transfer exhibit higher energy barriers on *T*r-Pt/TiO_2 (TS2 at 1.19 eV) relative to r*T*-Pt/TiO_2, indicating greater kinetic challenges in these processes. Conversely, the energy required for the dissociative adsorption of hydrogen onto Pt is lower for r*T*-Pt/TiO_2 (~0.56 eV), aligning with findings from H_2-TPD analyses and suggesting enhanced hydrogen dissociation capabilities crucial for promoting NEC hydrogenation. Integration of experimental data and DFT calculations underscores the advantageous adsorption properties of air-roasted *T*r-Pt/TiO_2 samples for n-NEC species, owing to their SMSI-induced interfacial structures. Conversely, r*T*-Pt/TiO_2, activated by H_2 pretreatment prior to Pt loading, exhibits reduced adsorption capacity for the 6H-NEC intermediate, leading to competitive

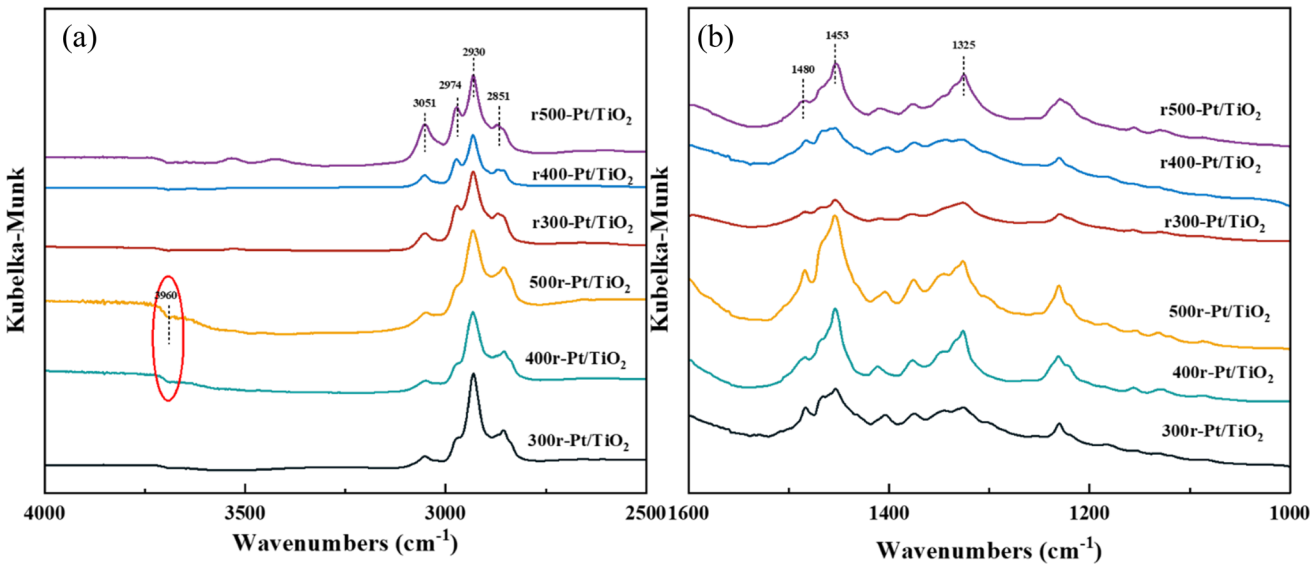

Fig. 7 12H-NEC-DRIFT spectra of the samples as indicated in panels ((a) 4000–2500 cm^{-1}, (b) 1200–2000 cm^{-1}).

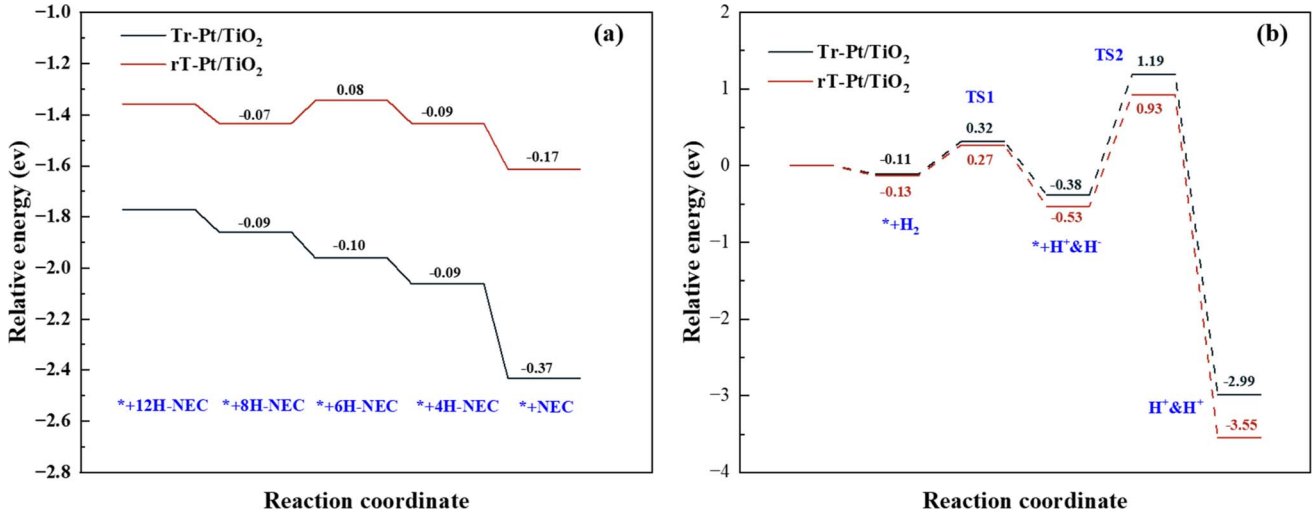

Fig. 8 (a) Adsorption energy for related intermediates on the samples and (b) dissociation and synthesis of hydrogen on sample models.

adsorption with 8H-NEC and higher energy barriers in the dehydrogenation pathway. For the reverse reaction of NEC hydrogenation, r*T*-Pt/TiO_2 demonstrates early Ti^{4+} activation, mitigating SMSI effects post-Pt loading and facilitating easier H_2 adsorption and dissociation. This unique interface configuration lowers energy barriers to H_2 dissociation, thereby promoting efficient hydrogenation processes. Integration of experimental data and DFT calculations underscores the advantageous adsorption properties of air-roasted *T*r-Pt/TiO_2 samples for n-NEC species, owing to their SMSI-induced interfacial structures. Conversely, r*T*-Pt/TiO_2, activated by H_2 pretreatment prior to Pt loading, exhibits reduced adsorption capacity for the 6H-NEC intermediate, leading to competitive adsorption with 8H-NEC and higher energy barriers in the dehydrogenation pathway. For the reverse reaction of NEC hydrogenation, r*T*-Pt/TiO_2 demonstrates early Ti^{4+} activation, mitigating SMSI effects post-Pt loading and facilitating easier H_2 adsorption and dissociation. This unique interface configuration lowers energy barriers to H2 dissociation, thereby promoting efficient hydrogenation processes.

4. Conclusion

In this study, two distinct series of catalyst samples, r*T*-Pt/TiO_2 and *T*r-Pt/TiO_2, were synthesized through treatments of P25 with contrasting atmospheres (H_2 and air), and subsequently applied to cyclic hydrogen storage reactions involving 12H-NEC dehydrogenation and NEC hydrogenation. The investigation focused on understanding the SMSI effects on these catalysts using a combination of experimental techniques and DFT calculations. The results revealed that the SMSI effect was weaker on the r*T*-Pt/TiO_2 surfaces compared to the *T*r-Pt/TiO_2 series. Specifically, in the r*T*-Pt/TiO_2 samples, Pt NPs were less encapsulated by TiO_x during hydrogen reduction. This phenomenon was attributed to the early activation of Ti^{4+} species on the TiO_2 surface following H_2 reduction of P25, which induced premature oxygen vacancy formation. Consequently, further reduction and encapsulation of Pt NPs became challenging, and Pt tended to deposit onto defective oxygen sites created by hydrogen treatment. In contrast, the air-treated P25 surfaces maintained stable hydroxyl (OH) and Ti–O structures without defects, facilitating the formation of a robust Ti–O–Pt structure upon Pt loading. This led to a stronger SMSI in the *T*r-Pt/TiO_2 samples, particularly evident at higher Pt reduction temperatures. Both series of catalysts, r*T*-Pt/TiO_2 and *T*r-Pt/TiO_2, were evaluated in the NEC hydrogen storage reactions. The *T*r-Pt/TiO_2 series exhibited superior performance in the 12H-NEC dehydrogenation reaction, highlighting its enhanced catalytic activity for releasing hydrogen. Conversely, the r*T*-Pt/TiO_2 series demonstrated better activity in the NEC hydrogenation reaction, indicating its proficiency in hydrogen uptake and storage. Experimental findings and DFT calculations concurred that the stronger SMSI in the *T*r-Pt/TiO_2 series facilitated an interfacial structure conducive to H_2 spillover and favorable adsorption of dehydrogenation intermediates. Conversely, the weaker SMSI in the r*T*-Pt/TiO_2 series promoted H_2 dissociation and uptake, thereby favoring the adsorption of hydrogenation intermediates. In conclusion, this study introduces a straightforward strategy to manipulate the SMSI between Pt and TiO_2 by pre-treating TiO_2 with different atmospheres prior to Pt loading. This approach not only provides insights into optimizing catalyst design for enhanced hydrogen storage applications using NEC but also opens new avenues for advancing catalytic strategies in renewable energy technologies.

Data availability

The data supporting this article have been included as part of the ESI.†

Conflicts of interest

The authors declare no competing financial interest.

Acknowledgements

Support from the National Natural Science Foundation of China (21576291) and from the Fundamental Research Funds for the Central Universities (23CX03007A) is gratefully acknowledged.

References

1 Z. Abdin, A. Zafaranloo, A. Rafiee, W. Mérida, W. Lipiński and K. R. Khalilpour, *Renewable Sustainable Energy Rev.*, 2020, **120**, 109620.
2 J. Yan, *Nat. Clim. Change*, 2018, **8**, 560–561.
3 J. O. Abe, A. P. I. Popoola, E. Ajenifuja and O. M. Popoola, *Int. J. Hydrogen Energy*, 2019, **44**, 15072–15086.
4 E. L. González, F. I. Llerena, M. S. Pérez, F. R. Iglesias and J. G. Macho, *Int. J. Hydrogen Energy*, 2015, **40**, 5518–5525.
5 A. F. Dalebrook, W. Gan, M. Grasemann, S. Moret and G. Laurenczy, *Chem. Commun.*, 2013, **49**, 8735–8751.
6 G. Sdanghi, G. Maranzana, A. Celzard and V. Fierro, *Renewable Sustainable Energy Rev.*, 2019, **102**, 150–170.
7 T. Zhang, J. Uratani, Y. Huang, L. Xu, S. Griffiths and Y. Ding, *Renewable Sustainable Energy Rev.*, 2023, **176**, 113204.
8 P. T. Aakko-Saksa, C. Cook, J. Kiviaho and T. Repo, *J. Power Sources*, 2018, **396**, 803–823.
9 S. Lim, Y. Song, K. Jeong, J. H. Park and K. Na, *ACS Sustainable Chem. Eng.*, 2022, **10**, 3584–3594.
10 L. K. Macreadie, R. Babarao, C. J. Setter, S. J. Lee, O. T. Qazvini, A. J. Seeber, J. Tsanaktsidis, S. G. Telfer, S. R. Batten and M. R. Hill, *Angew. Chem., Int. Ed.*, 2020, **59**, 6090–6098.
11 H. Jorschick, M. Geißelbrecht, M. Eßl, P. Preuster, A. Bösmann and P. Wasserscheid, *Int. J. Hydrogen Energy*, 2020, **45**, 14897–14906.
12 B. Wang, T. yan Chang, Z. Jiang, J. jia Wei, Y. hai Zhang, S. Yang and T. Fang, *Int. J. Hydrogen Energy*, 2018, **43**, 7317–7325.
13 Z. Jiang, X. Gong, S. Guo, Y. Bai and T. Fang, *Int. J. Hydrogen Energy*, 2021, **46**, 2376–2389.
14 X. Yang, Y. Wu, H. Yu, M. Sun, J. Zheng, X. Li, W. Lin and Y. Wu, *Int. J. Hydrogen Energy*, 2020, **45**, 33657–33662.
15 M. Yang, C. Han, G. Ni, J. Wu and H. Cheng, *Int. J. Hydrogen Energy*, 2012, **37**, 12839–12845.
16 Y. Dong, M. Yang, P. Mei, C. Li and L. Li, *Int. J. Hydrogen Energy*, 2016, **41**, 8498–8505.
17 W. Xue, H. Liu, B. Mao, H. Liu, M. Qiu, C. Yang, X. Chen and Y. Sun, *Chem. Eng. J.*, 2021, **421**, 127781.
18 H. Liu, C. Zhou, W. Li, W. Li, M. Qiu, X. Chen, H. Wang and Y. Sun, *ACS Sustainable Chem. Eng.*, 2021, **9**, 5260–5267.
19 M. Amende, C. Gleichweit, S. Schernich, O. Höfert, M. P. A. Lorenz, W. Zhao, M. Koch, K. Obesser, C. Papp, P. Wasserscheid, H. P. Steinrück and J. Libuda, *J. Phys. Chem. Lett.*, 2014, **5**, 1498–1504.
20 M. Yang, Y. Dong, S. Fei, H. Ke and H. Cheng, *Int. J. Hydrogen Energy*, 2014, **39**, 18976–18983.
21 C. Wan, Y. An, F. Chen, D. Cheng, F. Wu and G. Xu, *Int. J. Hydrogen Energy*, 2013, **38**, 7065–7069.
22 Z. Jiang, S. Guo and T. Fang, *ACS Appl. Energy Mater.*, 2019, **2**, 7233–7243.
23 M. Zhu, L. Xu, L. Du, Y. An and C. Wan, *Catalysts*, 2018, **8**, 638.
24 Z. Liu, Z. Feng and X. Bai, *Colloids Surf., A*, 2023, **676**, 132277.
25 B. Wang, S. yuan Wang, S. han Lu, P. ya Li and T. Fang, *Fuel*, 2023, **339**, 127338.
26 C. Dong, Z. Gao, Y. Li, M. Peng, M. Wang, Y. Xu, C. Li, M. Xu, Y. Deng, X. Qin, F. Huang, X. Wei, Y. G. Wang, H. Liu, W. Zhou and D. Ma, *Nat. Catal.*, 2022, **5**, 485–493.
27 B. Wang, Y. T. Chen, T. Y. Chang, Z. Jiang, Z. Q. Huang, S. Y. Wang, C. R. Chang, Y. S. Chen, J. J. Wei, S. Yang and T. Fang, *Appl. Catal., B*, 2020, **266**, 118658.
28 H. Meng, Y. Yang, T. Shen, Z. Yin, J. Zhang, H. Yan and M. Wei, *ACS Catal.*, 2023, **13**, 9234–9244.
29 Z. Jiang, X. Gong, B. Wang, Z. Wu and T. Fang, *Int. J. Hydrogen Energy*, 2019, **44**, 2951–2959.
30 X. Gong, Z. Jiang and T. Fang, *Int. J. Hydrogen Energy*, 2020, **45**, 6838–6847.
31 B. Wang, S. han Lu, S. yuan Wang, P. ya Li and T. Fang, *Appl. Surf. Sci.*, 2023, **618**, 156558.
32 Z. Yang, L. Li, X. Liu, X. Yang, H. Xiong, R. Zhang, Z. Jiang and T. Fang, *Chem. Eng. J.*, 2023, **474**, 145896.
33 M. S. Kim, S. H. Chung, C. J. Yoo, M. S. Lee, I. H. Cho, D. W. Lee and K. Y. Lee, *Appl. Catal., B*, 2013, **142–143**, 354–361.
34 J. Lin, T. Sun, M. Li, J. Yang, J. Shen, Z. Zhang, Y. Wang, X. Zhang and X. Wang, *J. Catal.*, 2019, **372**, 8–18.
35 R. Wang, N. Sakai, A. Fujishima, T. Watanabe and K. Hashimoto, *J. Phys. Chem. B*, 1999, **103**, 2188–2194.
36 N. L. Wu, M. S. Lee, Z. J. Pon and J. Z. Hsu, *J. Photochem. Photobiol., A*, 2004, **163**, 277–280.
37 E. Serwicka, *Colloids Surf.*, 1985, **13**, 287–293.
38 T. W. van Deelen, C. Hernández Mejía and K. P. de Jong, *Nat. Catal.*, 2019, **2**, 955–970.
39 Z. Luo, G. Zhao, H. Pan and W. Sun, *Adv. Energy Mater.*, 2022, **12**, 1–15.
40 K. Fujiwara, U. Müller and S. E. Pratsinis, *ACS Catal.*, 2016, **6**, 1887–1893.
41 S. Sun, X. Wu, Z. Huang, H. Shen, H. Zhao and G. Jing, *Chem. Eng. J.*, 2022, **435**, 135035.
42 J. C. Parker and R. W. Siegel, *Appl. Phys. Lett.*, 1990, **945**, 943–945.
43 J. Zheng, L. Liu, G. Ji, Q. Yang, L. Zheng and J. Zhang, *ACS Appl. Mater. Interfaces*, 2016, **8**, 2–9.
44 H. Huang and D. Y. C. Leung, *J. Catal.*, 2011, **280**, 60–67.
45 O. S. Alexeev, S. Y. Chin, M. H. Engelhard, L. Ortiz-Soto and M. D. Amiridis, *J. Phys. Chem. B*, 2005, **109**, 23430–23443.
46 M. A. Aramendía, J. C. Colmenares, A. Marinas, J. M. Marinas, J. M. Moreno, J. A. Navío and F. J. Urbano, *Catal. Today*, 2007, **128**, 235–244.
47 M. Y. Byun, Y. E. Kim, J. H. Baek, J. Jae and M. S. Lee, *RSC Adv.*, 2022, **12**, 860–868.
48 H. Gao, W. Xu, H. He, X. Shi, X. Zhang and K. ichi Tanaka, *Spectrochim. Acta, Part A*, 2008, **71**, 1193–1198.
49 G. J. Kim, D. W. Kwon and S. C. Hong, *J. Phys. Chem. C*, 2016, **120**, 17996–18004.

50 Z. Hou, Y. Zhu, H. Chi, L. Zhao, H. Wei, Y. Xi, L. Ma, X. Feng and X. Lin, *Chin. J. Chem. Eng.*, 2024, **70**, 189–198.
51 J. Zhang, H. Wang, L. Wang, S. Ali, C. Wang, L. Wang, X. Meng, B. Li, D. S. Su and F. S. Xiao, *J. Am. Chem. Soc.*, 2019, **141**, 2975–2983.
52 B. Han, Y. Guo, Y. Huang, W. Xi, J. Xu, J. Luo, H. Qi, Y. Ren, X. Liu, B. Qiao and T. Zhang, *Angew. Chem., Int. Ed.*, 2020, **59**, 11824–11829.
53 A. Pozio, Z. Jovanovic and S. Tosti, *Materials*, 2019, **12**, 3160.
54 N. Schreiter, J. Kirchner and S. Kureti, *Catal. Commun.*, 2020, **140**, 105988.
55 M. Yang, Y. Dong, S. Fei and H. Ke, *Int. J. Hydrogen Energy*, 2014, **39**, 18976–18983.
56 X. Gong, Z. Jiang and T. Fang, *Int. J. Hydrogen Energy*, 2020, **45**, 6838–6847.
57 Z. Feng, Y. Wang and X. Bai, *Environ. Sci. Pollut. Res.*, 2022, **29**, 39266–39280.
58 M. Amende, S. Schernich, M. Sobota, I. Nikiforidis, W. Hieringer, D. Assenbaum, C. Gleichweit, H. J. Drescher, C. Papp, H. P. Steinrück, A. Görling, P. Wasserscheid, M. Laurin and J. Libuda, *Chem.—Eur. J.*, 2013, **19**, 10854–10865.
59 M. Amende, C. Gleichweit, K. Werner, S. Schernich, W. Zhao, M. P. A. Lorenz, O. Höfert, C. Papp, M. Koch, P. Wasserscheid, M. Laurin, H. P. Steinrück and J. Libuda, *ACS Catal.*, 2014, **4**, 657–665.
60 M. Sobota, I. Nikiforidis, M. Amende, B. S. Zanón, T. Staudt, O. Höfert, Y. Lykhach, C. Papp, W. Hieringer, M. Laurin, D. Assenbaum, P. Wasserscheid, H. P. Steinrück, A. Görling and J. Libuda, *Chem.—Eur. J.*, 2011, **17**, 11542–11552.